

Distinction between Energetic Inhomogeneity and Geometric Non-Uniformity of Ion Insertion Electrodes Based on Complex Impedance and Complex Capacitance Analysis

M. D. Levi* and D. Aurbach

Department of Chemistry, Bar-Ilan University, Ramat-Gan 52900, Israel

Received: September 16, 2004; In Final Form: November 17, 2004

Electrochemical insertion of Mg ions into Mo_6S_8 Chevrel phase is a unique, model system for studying the nature of the energetic inhomogeneity of the host sites suitable for ions accommodation. We show that the two energy state model can be successfully used for describing the very specific Mg ions insertion kinetics into the host, in particular, as relates to a drastic increase of Mg ions mobility in the vicinity of the critical potential of 1.25 V (vs Mg). This is accompanied by very pronounced changes of the impedance spectra. On the other hand, similar behavior of impedance spectra could be obtained for geometrically nonhomogeneous intercalation electrodes, comprising a distribution of thicknesses. One can frequently meet both these cases in practice for a vast variety of intercalation electrodes (e.g., for lithiated graphite, composite Li_xMO_2 , $\text{M} = \text{Mn, Ni, Co, etc.}$). In this paper, we developed a methodology aimed at a reliable distinction between the two alternatives, based on complex impedance and complex capacitance analysis.

1. Introduction

Electrochemical impedance spectroscopy (EIS) is one of the most important, highly resolved electroanalytical techniques which may provide a unique information about the nature of electrode processes related to a wide range of time constants (demonstrated in terms of frequencies in EIS).^{1–18} The main problem appearing in practical application of this technique is its ambiguity: many physically different processes or separate stages of a more complicated process show similar features in terms of impedance spectroscopy. For classical electrochemical systems including processes such as electron-transfer, diffusion, and adsorption of reacting species, the distinction between them may be easy if all the adsorption sites have the same energy, i.e., the electrode surface is energetically homogeneous. The processes occurring in practical ion-insertion electrodes are much more complicated compared to the above classical systems, at least in two important aspects: (i) the host sites, in which ions are accommodated, may have considerably different energy and different activation barriers although the thickness of the electrode (through which solid-state diffusion takes place) is constant,^{19–21} or, alternatively, (ii) the intercalation sites are identical but the intercalation electrode is geometrically non-uniform, i.e., it is characterized by a distributed thickness and (or) particles size.^{22,23} Since one may frequently meet both these cases in practice, it is important to elaborate approaches which allow fast and reliable distinction between these alternative cases.

We have recently showed^{24–26} that the electrochemical insertion of Mg ions into Mo_6S_8 Chevrel phase in etherial solutions of Mg alkyl aluminum chloride complexes is a unique, model system for studying energetic inhomogeneity of the host sites which influences the nature of the electrochemical intercalation reactions. Deep traps with extremely slow intrinsic kinetics are very characteristic of the initial Mg ions insertion and final deinsertion to (from) Chevrel phase electrodes.^{24–26} In the

present paper, we show that the two energy state model of Bisquert et al.^{19,20} can help to understand the Mg ions insertion kinetics into Mo_6S_8 (Chevrel phase) electrodes and, in particular, in describing the drastic increase of Mg ions mobility occurring in the vicinity of a critical potential around 1.25 V (vs Mg).

On the other hand, we have recently shown²³ that spatial distribution of the thicknesses of porous electrodes results in an impedance behavior, which is qualitatively similar to that predicted by the two-energy state model. In the present paper, we deal with the fine details related to the impedance spectra obtained from unique insertion electrodes, discuss the application of appropriate modeling to these spectra and demonstrate the analysis of complex capacitance diagrams and frequency dependences of the real and the imaginary components of the complex capacitance as very useful tools for understanding the complicated impedance behavior of composite intercalation electrodes.

2. Experimental Section

The experimental details related to EIS characterization of Mg ions insertion into the Chevrel phase electrodes have been already reported.²⁶ The electrolyte solutions for Mg insertion studies included Mg salts of the general formula $\text{Mg}(\text{AlCl}_{(4-n)}\text{R}_n)_2$ (with R = alkyl group), possessing a relatively high anodic stability, dissolved in THF. Their preparation and properties were already reported.²⁷ 0.25 M $\text{Mg}(\text{AlCl}_2\text{BuEt})_2/\text{THF}$ solution (DCC/THF) was used as the electrolyte. The cathodes comprised the following components: 6 to 10 mg Mo_6S_8 , 10% carbon black and 10% PVdF (by weight), coated onto $1 \times 1 \text{ cm}^2$ stainless steel foils. Strips of Mg foil served as counter and reference electrodes. The cells were operated under highly pure argon atmosphere in M.Braun Inc. gloveboxes and were thermostated at different temperatures, with an accuracy of $\pm 0.5^\circ\text{C}$.

For detailed electrochemical impedance characterizations of Mg ions insertion into Mo_6S_8 we used a computerized potentiostat-galvanostat Eco Chemie Model 20 Autolab, supplied with

* To whom correspondence should be addressed. E-mail: levimi@mail.biu.ac.il. Tel: (972-3)531 88 32. Fax: (972-3)535 12 50/.

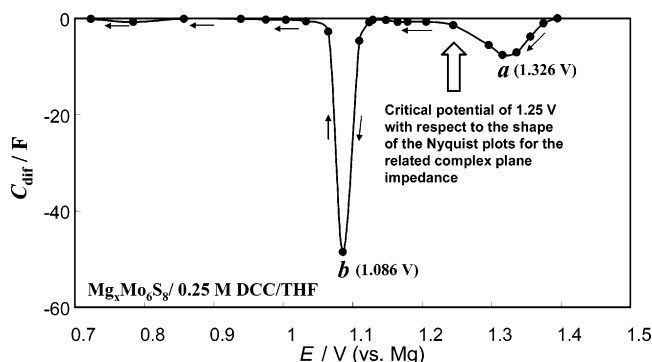


Figure 1. Plot of the equilibrium differential intercalation capacitance, C_{dif} vs. potential, E , obtained by PITT for Mg ions insertion into composite electrodes comprising the Chevrel phase compound as their active mass. The potentials of the cathodic peaks “a” and “b” as well as the critical potential of 1.25 V (with respect to the related Nyquist plots shown in Figure 2a) are indicated. THF solutions contained 0.25 M $\text{Mg}(\text{AlCl}_2\text{EtBu})_2$ complex (DCC/THF solution).

a FRA module. The collection of data was controlled by the GPES Version 4.8 Eco Chemie B. V. Software (Utrecht, The Netherlands). The electrodes' impedance was measured between 60 kHz and 5 mHz (in this order) after a complete equilibration of the electrodes at a variety of predefined potentials. High-resolution spectra were measured around a large number of equilibrium potentials in order to identify processes and states of interest. The impedance spectra collected for the Chevrel phase related to well-cycled electrodes, to exclude possible irreversible processes or processes with temporary slow dynamics. Real and imaginary parts of the complex capacitance, $C^* = (j\omega Z)^{-1}$ was derived from the experimental impedance plots, $-Z''$ vs Z' (representing imaginary and real parts of the impedance), using the following obvious equations

$$\text{Re}(C^*) = C' = \frac{C_{\text{sq}}}{(1 + \omega^2 R_{\text{sq}}^2 C_{\text{sq}}^2)} \quad (1a)$$

$$\text{Im}(C^*) = C'' = -j \frac{\omega R_{\text{sq}} C_{\text{sq}}^2}{(1 + \omega^2 R_{\text{sq}}^2 C_{\text{sq}}^2)} \quad (1b)$$

where $R_{\text{sq}} = Z'$ and $C_{\text{sq}} = -(\omega Z'')^{-1}$.

Theoretical impedance and capacitance plots both for a single trap and geometric nonuniformity models were calculated according to equations described in the Results section.

3. Results

3.1. Specific Equilibrium and Kinetic Features of Mg Ions Insertion into Mo_6S_8 Chevrel Phase. Figure 1 shows the plot of equilibrium differential intercalation capacitance, C_{dif} vs potential, E (measured vs Mg reference electrode in the same solution) obtained by potentiostatic intermittent titration (PITT) of a composite Chevrel phase electrode in DCC/THF solutions. It is seen that the insertion process proceeds in two steps: two cathodic peaks (“a” and “b”) appear on the C_{dif} vs E plot at 1.326 and 1.086 V, respectively. The ratio between the charge related to peaks “a” and “b” was close to 0.75–0.85. This picture is typical of the Mg ions insertion for repeated discharges during consecutive cycling (except for the first discharge, for more details see ref 24). Accurate galvanostatic measurements show that during initial Mg ions insertion into Mo_6S_8 electrodes (i.e., for the first discharge) the ratio between the inserted amounts of charge for the two processes was higher, close to 1:1, thus corresponding to $\text{Mg}_1\text{Mo}_6\text{S}_8$ and $\text{Mg}_2\text{Mo}_6\text{S}_8$ for the

steps “a” and “b” respectively. In contrast, the first Mg ions deinsertion (i.e., oxidation) is accompanied by irreversible trapping of Mg ions, so that the pristine Mo_6S_8 phase could not be recovered at the end of the deinsertion, leaving 15–25% of the stoichiometric amount of the $\text{Mg}_1\text{Mo}_6\text{S}_8$ phase inaccessible at any practical rate of charge and discharge at room temperature, independent of the cycle number.²⁴ An interesting feature of the thermodynamics and the kinetics of Mg ions insertion into Mo_6S_8 is that the amount of the inserted charge for the second stage (peak “b”) is usually exactly half of the theoretical specific capacity of this electrode.²⁴ These features are explained by incomplete Mg ions deinsertion at the end of the $\text{Mg}_1\text{Mo}_6\text{S}_8$ charge due to very low mobility of these divalent ions. The practical absence of the cations in the shallow sites (in the considered potential range), results in a very low ionic conductivity. Single-charged lithium ions are much more mobile in the same host compared to that of Mg ions, and, hence, can be completely removed at the end of charge.²⁴ Note, however, that since the charge under the peak “b” is a half of the theoretical capacity, this means that the final two electrons of the total 4 electrons (and, hence, the second Mg ion in $\text{Mg}_x\text{Mo}_6\text{S}_8$) are also transferred to the $\text{Mg}_1\text{Mo}_6\text{S}_8$ units containing immobile Mg ions. This should be related to a very specific nature of both kinds of sites for inserted cations in Mo_6S_8 Chevrel compound (sites A and B), with account of divalent character of the Mg ions, and the specific transition of these ions from sites A to sites B in the vicinity of $x = 1$, as is later discussed.

Figure 2a shows that in the potential range from the beginning of Mg ions insertion and then within the potential range related to the peak “a” in Figure 1, the electrode impedance is very high. At the potential of 1.25 V, related to the end of magneziation of Mo_6S_8 to $\text{Mg}_1\text{Mo}_6\text{S}_8$ (marked by an arrow in Figure 1), the electrode's impedance drastically decreases, showing a distinctive characteristic behavior, namely, a pronounced decrease in the diameter of the low-frequency semicircle (LFS), which is separated, in the medium frequency range, from the high-frequency semicircle (HFS), by a Warburg-type element. The small HFS, appearing in the Nyquist plots of these electrodes, was previously related to a combined effect of adsorbed Mg-containing species and a slow interfacial charge transfer,²⁶ and will not be further discussed in the present paper. The Warburg impedance in the medium-frequency domain becomes, as the potential decreases, more like a Gerischer-type impedance^{21,26} (see also subsection 3.2), transforming, in the limit of low frequencies, into a sloping, capacitive line (Figure 2a). All of the above three types of impedance, namely, the Warburg (or the Gerischer) impedance, the LFS and the sloping, capacitive line, can be associated with characteristic frequencies, f_0 , f_t , and f^* , respectively, as shown by the solid circles in Figure 2a. Their physical meaning is discussed later.

Since one of the aims of this paper is to describe the characteristic potential dependence of the impedance of magneziated Chevrel phase by a single trap model (see subsection 3.2), it is worth, according to Bisquert et al.,^{19,20} to present the data in the form of complex capacitance, C^* . Its real and imaginary values, C' and C'' , respectively, were calculated according to eqs 1a and 1b. Such a presentation emphasizes the medium (Figure 2c) and the low-frequency domains of C^* (Figure 2b), facilitating elucidation of the capacitive contributions from insertion sites of different interactions (i.e., different energetics^{19,20}). The low-frequency domains of the C'' vs C' plots for all the relevant potentials reveal the curves close to semicircles, which correspond to sloping, capacitive lines in the related Nyquist plots. The fine differences between the curves

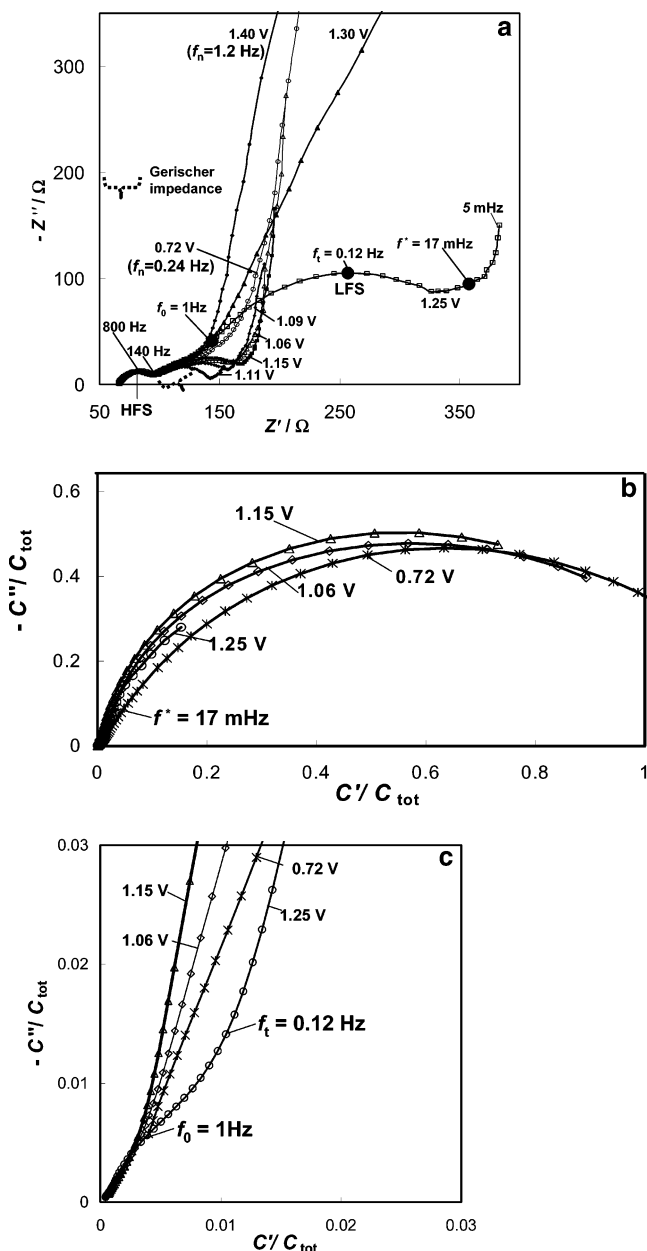


Figure 2. Nyquist plots, $-Z''$ vs Z' (a), and the related complex capacitance presentation, C'' vs C' with $C^* = C' + jC''$ (b and c) for Mg ions insertion into Chevrel phase electrodes in DCC/THF solution, measured at different potentials both above and below the critical potential of 1.25 V. Panel "c" is an enlarged view of the complex capacitance plot in the medium-to-high frequency domain of the capacitance spectra. Three characteristic frequencies, f_0 , f_t , and f^* in the high, medium and low frequency domains of the impedance and capacitance spectra, respectively, measured at the critical potential of 1.25 V, are marked by large filled circles (for their meaning, see text related to model curves in Figures 6a and 7a).

in Figure 2b are discussed later. A straight line of 45° slope is seen in Figure 2c in the high-frequency limit. For most of the potentials, the C'' vs C' plots appear as sloping lines, whereas at the critical potential of 1.25 V a clear deviation toward an arc is observed. The characteristic frequency, f_0 marks the beginning of the arc, whereas f_t is the characteristic frequency which relates to its transformation to the LFS; f^* relates to the boundary between the LFS and the capacitive, vertical line.

Figure 3 presents frequency dependence of both quantities, C'' and C' (in logarithmic coordinates). The curves have the following characteristic features: (i) they tend to merge at high

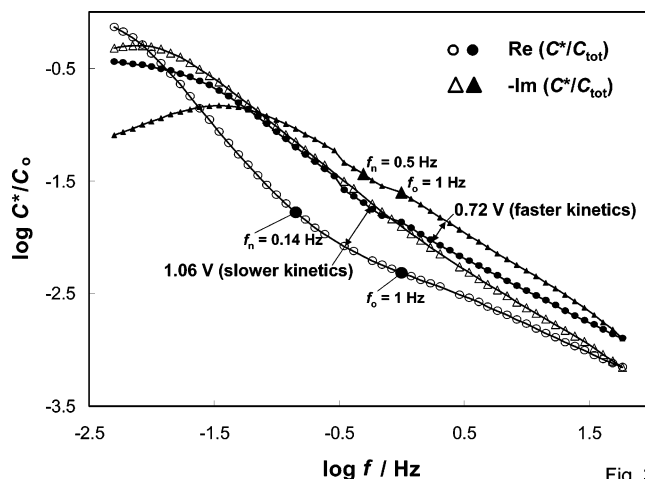


Fig. 3

Figure 3. Frequency-dependent real and imaginary parts of the complex capacitance C^* calculated from the impedance spectra of the Chevrel phase electrode (presented in Figure 2) at 1.06 and 0.72 V.

frequencies only: (ii) in the range of low frequencies, C'' has a maximum whereas C' reaches a plateau; (iii) the higher is the intercalation level (i.e., the lower is the potential) the broader is the segment formed by intersection of the plots of C'' and C' in the low frequency domain and the common line, marking their practical coincidence in the limit of very high frequencies; the separation between the characteristic frequencies $f_n = f^*$ and f_0 decreases with the increase in the intercalation level (precise meaning of f_n is clarified later, in subsection 3.2).

The single trap model presented in the following subsection, is aimed at a semiquantitative description of the nature of abrupt changes in Z and C^* close to the critical potential of 1.25 V.

3.2. A Single Trap Model for the Impedance and Complex Capacitance of $\text{Mg}_x\text{Mo}_6\text{S}_8$ Chevrel Phase Electrodes. The kinetic and the thermodynamic properties of a single trap model were recently studied by Bisquert et al.^{19,20} In the simplest case, namely, of a host with only two types of intercalation sites, we can suggest that they differ from each other by their energetics: "deep" sites A with high activation barriers and "shallow" sites B with lower activation barriers (see Figure 4a). Since the bottom of sites A are lower in energy compared to that of sites B, the former should be preferentially occupied at the beginning of ions insertion. The dynamics of occupation of sites A require the characteristic time of the insertion process to be sufficiently long (i.e., the related frequency should be low enough), to allow the ions to overcome the relatively high activation barriers. Note also that although in the range of potentials, which are thermodynamically favorable for the occupation of sites A, these dynamics imply also a *transient* occupation of the shallow sites with a lower activation barrier. Thus, the ions insertion kinetics should be dependent on the time duration (or the related frequency) of the probing potential (or current) perturbation, as well as on the temperature.

In Figure 4b, we show basic elements of crystal structure of the Chevrel phase (following ref 28): Mo_6 -clusters build octahedral units included in slightly distorted cubes of S_8 -anions. The sites for small ions accommodation are built by four neighboring sulfur anions of approximately tetrahedral symmetry: six such sites form an inner ring (close to the origin of the unit cell) perpendicular to the ternary axis whereas 6 other tetrahedral sites are located on both sides of the inner ring, forming an outer ring (see Figure 4b). We identify the sites belonging to the inner ring with deep sites A: a lower energy is reached due to their being close to the origin of the unit cell

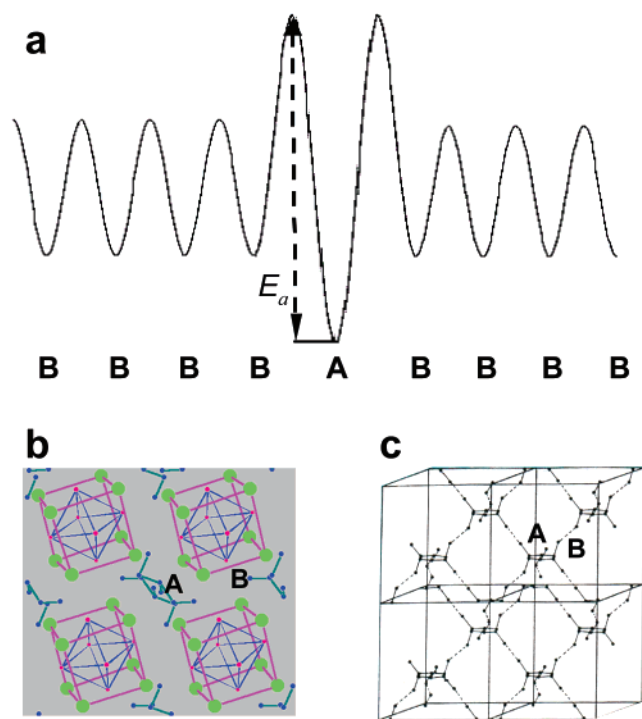


Figure 4. General schematic representation of the energy of the available sites for ions insertion into the host matrix according to the single trap model developed by Bisquert et al. (a).^{19,20} Sites A are traps with higher energy barriers and lower bottom energy compared to “shallow” sites B. E_a denotes the activation energy required to liberate the trapped ions, i.e., to transform them into the transition shallow sites. Panel “b” shows the crystal structure of the Chevrel phase²⁸ which comprises Mo_6 octahedra included inside slightly distorted cubes of sulfur anions (filled circles), inner and outer 6 sites rings (for the intercalating ions), which are identified with the trapping sites A and the more shallow sites B. Panel “c” is a simplified view of the crystal structure of panel “b” showing a three-dimensional network of sites A and B only (in order to simplify the view, the Mo_6 octahedra and the S_8 cubes were removed).²⁹

and the stabilization of the ground energy by the high electrostatic interaction of divalent Mg ions with two neighboring axial sulfur anions. Hence, sites A should be preferentially occupied at low intercalation level, x . As x is higher and becomes equal to 1 (i.e., in the vicinity of the critical potential of 1.25 V), all the inner rings contain one Mg ion. With further increase in x the inner rings cannot accommodate more Mg ions because of the short distance in the ring and a large electrostatic repulsion between two divalent cations; thus these cations occupy the sites of the outer ring (sites B). A part of three-dimensional network of sites A and B separated from host chalcogenide anions and Mo cations is shown in Figure 4c.²⁹

To apply the two-states (single trap) model for the insertion of Mg ions into the Chevrel phase in the most simplistic way, we take into consideration that the potential 1.25 V (marked by the arrow on the differential capacitance plot in Figure 1) has a clear feature of the *critical* potential, since it separates the spectra with the large and the small diameters on the related LFSs. Despite the very large change in C_{dif} along the second intercalation peak (and the corresponding change in x), the changes in the diameters of the related LFSs are surprisingly small compared to that for the preceding stage of the Mg ions insertion. Note that near the critical potential almost all sites A are occupied. We additionally assume that close to this potential, the activation barrier of the deep sites A decreases due to electrostatic repulsion between the divalent Mg ions, so that the initially trapped ions enhance their mobility. This means

that the shallow sites B become progressively more accessible (in a *transition* mode) whereas the ratio between the equilibrium concentrations of the deep and the shallow sites does not change very much with the potential (the critical potential 1.25 V is located between the major peaks “a” and “b” in Figure 1).

This situation is specific for the Mg ions insertion into Mo_6S_8 , in contrast to the very fast insertion of single-charged ions such as Li cations to the same host.^{24–26} The reason for this different behavior seems to be a higher ionicity of the Mg–S bond compared to the Li–S bond. On the other hand, the difference between the transition and the equilibrium sites for Mg ions insertion outlined above becomes even clearer when comparing the insertion process into Mo_6S_8 and Mo_6Se_8 Chevrel phases.³⁰ The thermodynamics of Mg ions insertion into these hosts are very similar (two-steps charge-transfers, the same total *equilibrium* intercalation capacitance). However, Mg ions transport in the Mo_6Se_8 host is very fast within the entire range of intercalation levels even at room temperature. Thus, in this case, deep sites with high potential barriers are not formed due to a more covalent character of the Mg–Se bonds compared to that of the Mg–S bonds in the transition state (generally, a link between the covalent interactions of the inserted ions with the host anions in the transition state and the transport characteristics of these ions is well-documented in solid-state chemistry³¹).

We now apply the two-state model for the insertion of Mg ions into the Mo_6S_8 Chevrel phase. As was shown by Bisquert et al.,^{19,20} this model results in a complex impedance ($Z(s)$) that can be conveniently presented as a function of the angular frequency ($\omega = 2\pi f$) in the form

$$Z(s) = R_o(\omega_n^*(s)/s)^{1/2} \coth[(s/\omega_n^*(s))^{1/2}] \quad (2)$$

where $s = j\omega$, and the diffusion resistance R_o (related to the motion of the intercalated ions between the shallow sites) is linked to the corresponding diffusion coefficient, D_o , through the intercalation capacitance of the shallow sites, C_o , and the characteristic frequency, ω_o

$$\omega_o/2\pi = \frac{D_o}{L^2} = \frac{1}{R_o C_o} \quad (3)$$

Here, L is the electrode thickness. According to the two state model,^{19,20} the intercalated ions move by ordinary diffusion mechanism between the shallow sites, interacting, at the same time, with the deep sites and becoming immobilized for a lapse of time. The characteristic frequency, related to ion trapping in the deep sites and release from them, ω_t , defines an effective, frequency dependent complex diffusion coefficient, $D_n^*(s)$, through the ratio between the intercalation capacitances due to the deep and the shallow sites, C_{trap} and C_o , respectively

$$D_n^*(s) = \frac{(\omega_o/2\pi)L^2}{1 + \left[1 + \frac{s}{\omega_t}\right]^{-1} \frac{C_{\text{trap}}}{C_o}} \quad (4)$$

Note also that the diffusion motion coupled with ions trapping in the deep sites can be presented by a characteristic frequency as follows^{19,20}

$$\omega_n^*(s)/2\pi = D_n^*(s)/L^2 \quad (5)$$

with $D_n^*(s)$ obtained from eq 4. Thus, defined $\omega_n^*(s)$ should be inserted in eq 2 for the final calculation of the electrode

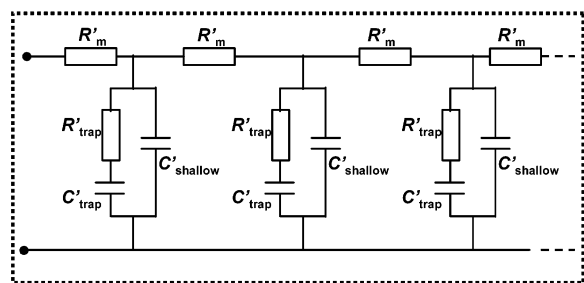


Figure 5. Equivalent circuit analogue for the process of trapping Mg ions in the Chevrel phase using a semi-infinite transmission line consisting of a distributed resistance R'_m with a transverse element presented by two parallel branches due to a distributed shallow capacitance, C'_shallow , and a distributed serial RC combination of the trapped resistance and the capacitance, R_trap and C_trap , respectively.

impedance for the case of the diffusion coupled with ion trapping.

The traps kinetics relates to the characteristic frequency ω_t , which can be expressed through the trap capacitance, C_trap and trap resistance, R_trap

$$\omega_t/2\pi = \frac{1}{R_\text{trap}C_\text{trap}} \quad (6)$$

R_trap characterizes the transition of ions between shallow and deep sites having the meaning of a homogeneous charge-transfer resistance.^{19,20} In cases of very slow trapping kinetics (R_trap is large), when a small frequency of the alternating voltage, ω , is used, so that $R_\text{trap} \ll (1/\omega C_\text{trap})$, the impedance response becomes completely capacitive. The capacitance at this frequency is then cumulative with respect to both types of intercalation sites

$$C_\text{tot} = C_o + C_\text{trap} \quad (7)$$

The impedance written in the form of eqs 2 can be better understood in terms of the transmission line representation (see Figure 5) with the two transverse branches in parallel, comprising the intercalation capacitance of the shallow sites, C_o , and the intercalation capacitance of the deep sites, C_trap , in series with the relevant kinetic parameter, namely, the trapping resistance, R_trap .

Modeling impedance spectra of an intercalation electrode with two different energy sites through eqs 2–7 requires four independent parameters: ω_o , ω_t , C_trap , and C_o . The main problem of the modeling is a reasonable guess of how these parameters may depend on the electrode potential (or intercalation level). Taking into account the above arguments on the transition between deep and shallow sites in the vicinity of the critical potential, we assumed that the only parameter, which changes with the potential, is the characteristic frequency of the trapping process, f_t . Since the ratio between the capacitances due to deep and shallow sites, C_trap/C_o , is considered to be constant in the vicinity of this transition, the charge-trapping resistance, R_trap , as follows from eq 6, is inversely proportional to f_t . The quantity f_t is assumed to increase with decreasing the electrode potential due to lowering the height of the activation barrier as a result of a drastic increase in the electrostatic repulsion between the Mg ions. For the purpose of a qualitative comparison between the experimental data and the model, we consider an augmentation of f_t by more than 3 orders of magnitude. The ratio C_trap/C_o was assumed to be 10, i.e., under the domination of deep sites over the shallow ones (consideration of the potential dependences of both capacitances, while complicates the

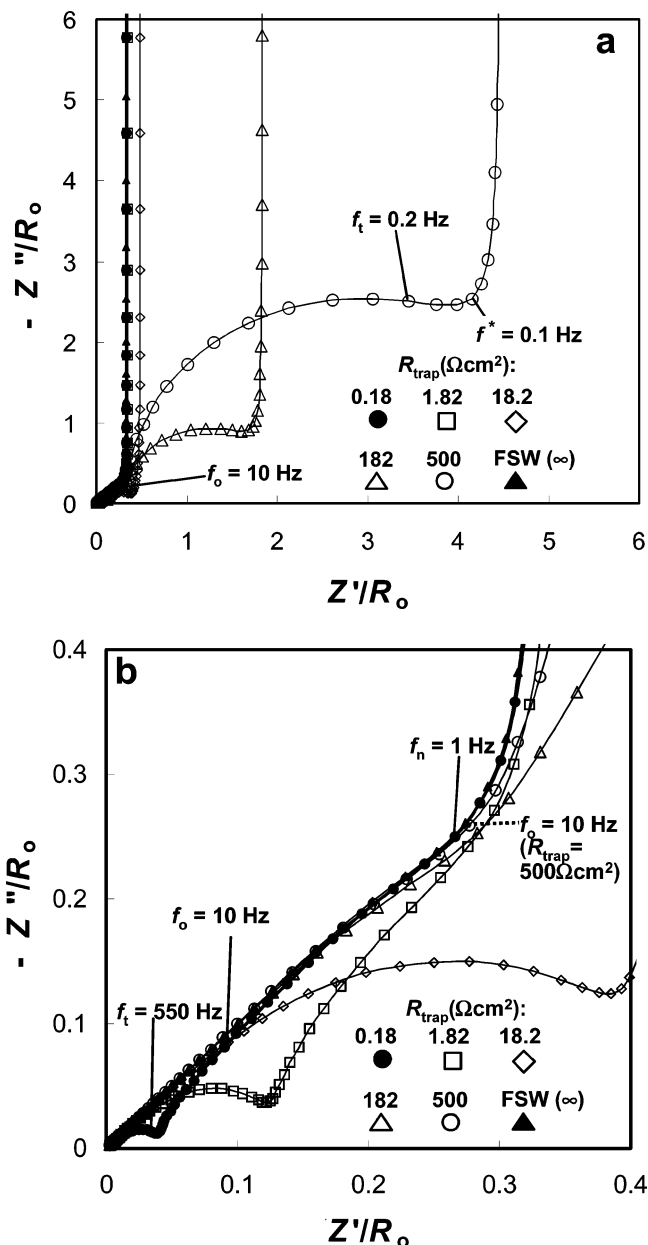


Figure 6. Nyquist plots obtained for a two sites (single trap) model with the use of eqs 8–13 for the whole frequency domain from 320 kHz to 0.1 mHz. (a) and the enlargement of the high-frequency domain (b). The following parameters were used: $R_o = 100 \Omega\text{cm}^2$, R_trap (as indicated), C_o and $C_\text{trap} = 0.001$ and 0.01 mFcm^{-2} , respectively, $f_o = 10 \text{ Hz}$. f_t and f^* (f_n) are indicated for the spectra related to $R_\text{trap} = 500$ and $0.18 \Omega\text{cm}^2$, respectively.

analysis, does not change qualitatively the effect of f_t on the electrode impedance).

Figure 6 shows theoretical impedance spectra calculated with the use of eqs 2–7 as a function of the parameter f_t (or, equivalently, as a function of the charge-trapping resistance, R_trap , as indicated in the figure). Panel “a” refers to the whole frequency domain whereas panel “b” enlarges, for clarity, the high frequency domain. The curve related to $R_\text{trap} = 500 \Omega\text{cm}^2$, has three characteristic frequencies, namely, f_o , f_t , and f^* (the latter was identified as the boundary frequency between the LFS and the low-frequency, capacitive line on the related impedance spectrum as indicated). It is seen that this case corresponds to very slow trapping kinetics of the initial Mg-ions insertion ($f_t \ll f_o$), thus the high-frequency impedance shows a pattern of a classical semi-infinite Warburg behavior (see Figure 6b and the

location of the characteristic frequency f_0 for $R_{\text{trap}} = 500 \Omega\text{cm}^2$ since at these high frequencies the diffusion of ions via the shallow sites is unperturbed by the slower trapping kinetics.^{19,20} At lower frequencies, the Mg ions are trapped, and the resulting LFS is formed by a parallel combination of C_0 and R_{trap} (see the equivalent circuit in Figure 5).

The decrease in the values of the parameter R_{trap} (i.e., the increase in f_i) obviously leads to a considerable decrease of the diameter of the LFS (see Figures 6a and b). As a result, the impedance spectra acquire a qualitatively new feature of a Gerischer-type impedance in the high-frequency domain, followed by a semi-infinite Warburg behavior, and finally, by vertical capacitive line as the frequency decreases. These new features of the relatively fast trapping kinetics, were first established by Bisquert et al.,²¹ and can be easily understood from the transmission line representation shown in Figure 5 and from the values of the characteristic frequencies f_i and f_0 : as the frequency becomes high, in addition to a high value of C_{trap} , the reactance related to C_{trap} is small compared to R_{trap} . In this case, the latter quantity is much less than R_0 , hence $f_i \gg f_0$ (see the values indicated in Figure 6b), and the concentration profile of the intercalated ions decays before the species reach the boundary at the current collector (the Gerischer impedance).²¹

This impedance spectrum related to the energetically heterogeneous intercalation electrode with relatively fast trapping kinetics has two semi-infinite Warburg regions with the different prefactors linked to f_0 and f_n at high and medium frequencies, respectively (see Figure 6b). When R_{trap} increases to very large values, the impedance response is reflected by the classical finite-space Warburg element (FSW) with one single characteristic frequency f_0 . Interestingly, analyzing the opposite case, when the trap resistance decreases virtually to zero (i.e., in the process of transition to the intercalation electrode with single energy sites) the impedance response, once again, will be reflected by FSW (see the equivalent circuit in Figure 5), with, however, lower frequency than the frequency typical of the shallow sites, $f_n < f_0$. This is because of coupling between the fast trapping kinetics of the deep sites and the ordinary diffusion of ions through the shallow sites. In the limit of low frequencies, the total capacitance $C_{\text{tot}} = C_0 + C_{\text{trap}}$ (see eq 7) is charged at the characteristic frequency $f_n < f_0$ since the ordinary diffusion through the shallow sites is slowed, e.g., by short-time residence of the inserted species in the deep sites.

It is important to understand the difference between the characteristic frequencies f^* and f_n for the systems with large and small R_{trap} , respectively: In the former case, the dynamics of deep and shallow sites exchanges is virtually uncoupled, the traps do not modify the Warburg diffusion of ions through the shallow sites at high frequencies. At lower frequencies, when only C_0 is relevant, this capacitance appears to be in parallel to R_{trap} , forming semicircles in the related impedance spectra (Figure 6a and b). However, a further decrease in frequency results in charging the total capacitance ($C_0 + C_{\text{trap}}$) at a characteristic frequency f^* , which does not relate to any of the diffusion-like mechanisms! In contrast, in case of fast trapping kinetics (R_{trap} is small) the low-frequency impedance is very close to an ordinary FSW diffusion with the characteristic frequency $f_n < f_0$ as outlined above. Comparison between the experimental impedance plots shown in Figure 2 and the theoretical ones for the single trap model (Figure 6, parts a and b) show their striking qualitative similarity.

Some ambiguity in distinguishing between the characteristic arcs of the Gerischer impedance and the LFS due to the ion trapping may appear in the case of small R_{trap} (see e.g., the curve

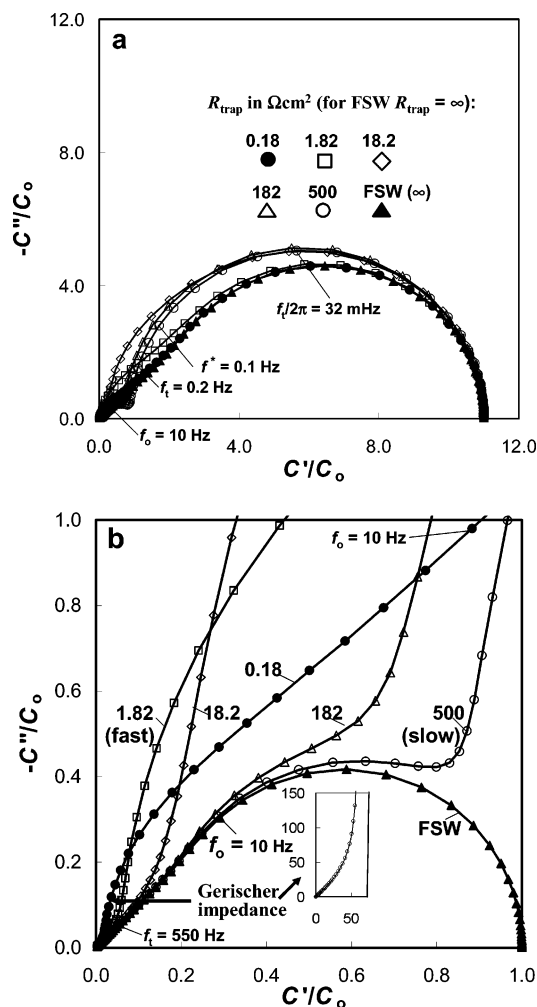


Figure 7. Theoretical complex capacitance plots corresponding to the model Nyquist plots for the two-sites, single trap model shown in Figure 6a and b (the characteristic frequencies in panels “a” and “b” refer to $R_{\text{trap}} = 500$ and $0.18 \Omega\text{cm}^2$, respectively). The inset in panel “b” represents a capacitance plot for a pure Gerischer-type impedance, which elements can be found as a high-frequency limit of the capacitance plots for small values of R_{trap} , as indicated.

with $R_{\text{trap}} = 0.18 \Omega\text{cm}^2$ in Figure 6b). The distinction between them can be visualized in the form of the complex capacitance diagrams, calculated from the impedance with the use of eq 1. C'' versus C' plots for the whole range of frequencies and R_{trap} are shown in Figure 7a (the plots in Figure 7b show the high-frequency domain only). The low-frequency features of the C''/C_0 versus C'/C_0 plots present a part of the semicircle, which is independent of the value of R_{trap} . The characteristic frequency values are marked in the plot related to $R_{\text{trap}} = 500 \Omega\text{cm}^2$ (Figure 7a). Comparing this plot with that for the FSW ($R_{\text{trap}} = \infty$) in Figure 7b, one can see that C''/C_0 can be easily found by extrapolating the medium-frequency semicircle toward lower frequencies. The high-frequency domain of the complex capacitance plot for $R_{\text{trap}} = 500 \Omega\text{cm}^2$ coincides with that for the FSW, reflected by a straight line of unit slope.

As the value of R_{trap} decreases, the length of the high-frequency straight line drastically reduces, causing an almost vertical increase in C''/C_0 as the frequency decreases (Figure 7b), then, in the limit of very low frequency, a semicircle is formed (Figure 7a). The transfer from the straight line of the unit slope to the vertical line for the imaginary part of the capacitance clearly manifests the appearance of the Gerischer impedance (more strictly, the related complex capacitance) at

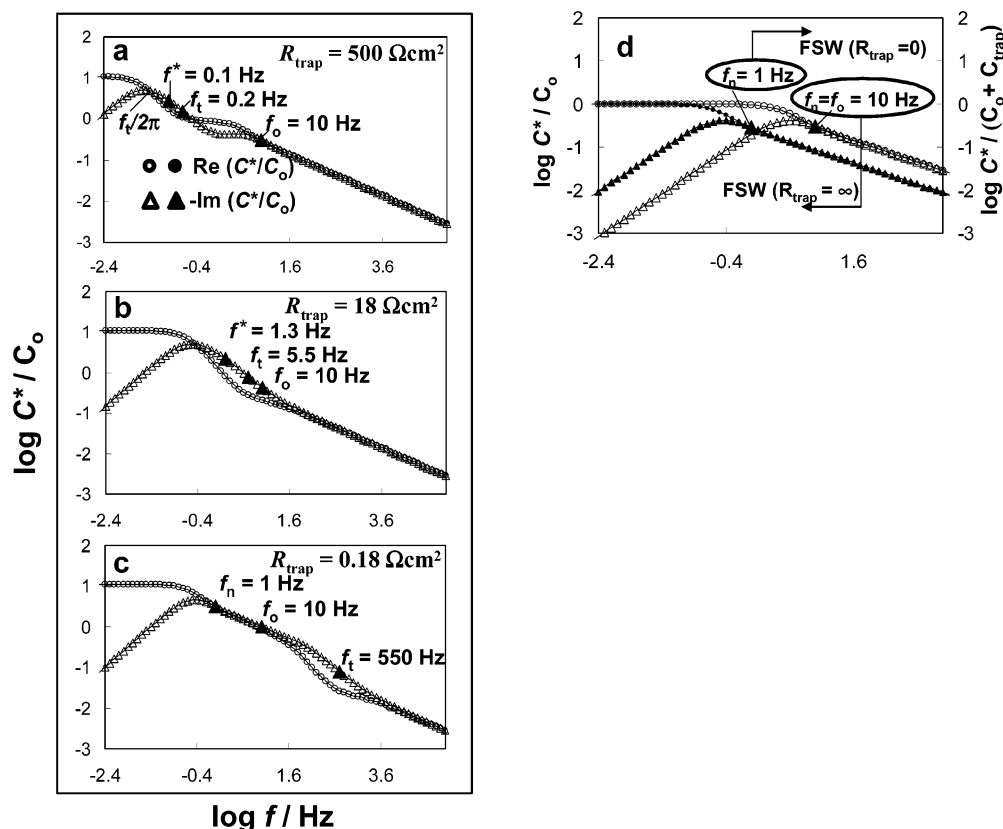


Figure 8. Plots of the real and the imaginary parts of the complex capacitance C^* as a function of frequency (in logarithmic scale) taken from the complex capacitance plots shown in Figure 7. R_{trap} in panels a–b is indicated. Panel “d” relates to the pure finite-space Warburg element with R_{trap} either 0 or ∞ as indicated.

the high frequencies. The inset in Figure 7b shows the plot of the complex capacitance for the pure Gerischer impedance, which is quite similar to the high-frequency parts of the plots for small values of R_{trap} .

Finally, Figures 8a–d show frequency dependences of the imaginary and real components of the complex capacitance with the characteristic frequencies marked by the solid triangles. These plots can be easily used for a visual determination of the energetic inhomogeneity of the sites in ion-insertion electrodes. It is instructive first to analyze the shape of the curves for the homogeneous case (Figure 8d). The plots (in logarithmic coordinates) are expressed by coinciding straight lines in the high-frequency domain, however, as the frequency decreases, in the vicinity of f_n , the imaginary part of C^* passes through a maximum, whereas its real part reaches a plateau at the same frequencies. Figure 8d clearly shows that the plots for the two FSW with $R_{\text{trap}} = \infty$ and $R_{\text{trap}} = 0$ are virtually the same curves shifted along the $\log f$ -axis by the ratio of the related f_n values.

At a small value of $R_{\text{trap}} = 0.18 \Omega\text{cm}^2$ (see Figure 8c), the low-frequency domain of the C''/C_o and C'/C_o vs frequency plots (characteristic frequency f_n) are very much similar to that of the FSW. However, at higher frequencies, a clear loop between both plots emerges with a “hump” on the plot of the imaginary capacitance and the two characteristic frequencies, f_o and f_t on its both sides. When higher values of R_{trap} are used for these calculations, this loop is shifted toward lower frequencies (see Figure 8b). Finally, at high values of R_{trap} , the loop is divided into two sub-loops, moving further toward lower frequencies (see Figure 8a): f_t and f_o change their positions with respect to the hump in the curve of C''/C_o vs frequency, as compared to the case for the small values of R_{trap} (compare with Figure 8c).

Comparison between the theoretical curves in Figures 7 and 8 and the related experimental plots in Figures 2 and 3 (for different values of potentials) show their close qualitative similarity, which supports our major assumption concerning the increase of the mobility (i.e., a decrease in the barrier energy) of the ions in the deep sites in the vicinity of the critical potential of 1.25 V.

3.3. Impedance and Complex Capacitance of Composite Electrodes Consisted of Distributed Porous Sublayers. In the previous sections, we dealt with a phenomenon of energetic nonuniformity of intercalation sites in host electrode materials. However, there is another very common source of nonuniformity in intercalation reactions related to the composite structure of the electrodes. Mg or Li ions insertion electrodes are usually composed of micron size particles bond to the current collector by a polymeric binder. In many cases, such electrodes are not uniform in their thickness or particle size, and such nonuniformities influence very strongly their impedance behavior. Hence, it is interesting to compare the impedance response due to nonuniformity in the energetics of the reaction sites in the host particles and the nonuniformity related to the composite structure of the electrodes.

In this subsection, we concentrate on the impedance and complex capacitance of an electrode composed of host particles of different sizes. For simplicity, we treat the case in which there are only two types of particles with two different radii, R_1 and R_2 . The electrode consists of two porous sublayers (thicknesses L_1 and L_2), as is shown in Figure 9a. The impedance behavior of single-layer porous electrodes has been recently analyzed by Meyers et al.,²² whereas the case of an electrode comprising nonuniformly stacked porous sublayers was treated by us, as reported earlier.²³ Here we supplement the analysis

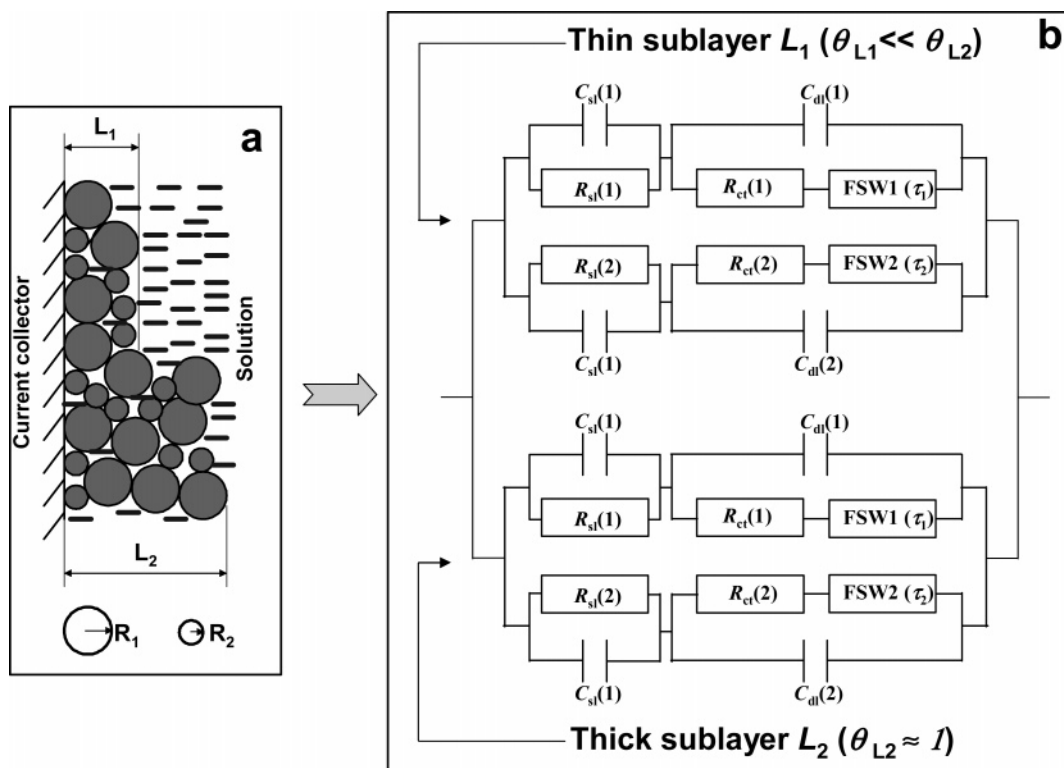


Figure 9. Sketch of a nonuniform composite electrode which comprises coatings of different thicknesses on the current collector (two porous sublayers, thicknesses L_1 and L_2) composed of particles (intercalating host) with two different radii (R_1 and R_2), panel “a”, and the corresponding equivalent circuit analogue, panel “b”.

of the impedance behavior of the electrode schematically shown in Figure 9a (which is qualitatively similar to the impedance behavior of the electrode containing shallow and deep sites) with the analysis of its complex capacitance.

The impedance of an individual particle which inserts/deinserts ions, $Z_{\text{part},i}$, can be presented in the following form^{22,23}

$$Z_{\text{part},i} = \frac{R_{\text{ct},i} + \frac{R_{\text{part},i}}{Y_{\text{s},i}}}{1 + j\omega C_{\text{dl},i} \left[R_{\text{ct},i} + \frac{R_{\text{part},i}}{Y_{\text{s},i}} \right]} + \frac{R_{\text{sl},i}}{1 + j\omega R_{\text{sl},i} C_{\text{sl},i}} \quad (8)$$

with the finite-space diffusion resistive element, $R_{\text{part},i}$, of the form:²²

$$R_{\text{part},i} = \frac{R_{\text{s},i}^2}{3D_o C_{\text{part},i}} = \frac{\tau_i}{3C_{\text{part},i}} \quad (9a)$$

$(1/Y_{\text{s},i})$ is a spherical analogue of the characteristic function of the angular frequency (ω) in the expression for a linear finite-space Warburg element:²²

$$\frac{1}{Y_{\text{s},i}} = \frac{\tanh(\sqrt{j\omega\tau_i})}{(\sqrt{j\omega\tau_i} - \tanh(\sqrt{j\omega\tau_i}))} \quad (9b)$$

Here, $C_{\text{part},i}$ stands for the limiting low-frequency capacitance of a spherical particle, $R_{\text{s},i}$ is the diameter of the spherical particle, D_o is the chemical diffusion coefficient, τ_i designates the related diffusion time constant, and ω was previously defined as the angular frequency of the alternative current. Subscript i denotes particles with different radii, e.g., either 1 or 2. Since intercalation electrodes, especially in Li salt solutions are

covered by surface films³² we have to take into account the surface films, parameters R_{sl} and C_{sl} in the above equations (related to the resistance of ions migration through the films and to the films capacitance, respectively). R_{ct} reflects interfacial charge transfer resistance (e.g., across the boundary between the surface films and the active mass), defined previously (note that R_{ct} and R_{sl} are the diameters of the MFS and HFS, respectively, which characterize the impedance spectra of these electrodes). $C_{\text{dl},i}$ is the interfacial double layer capacitance. The total admittance of an electrode comprising a mixture of two types of particles in terms of different size, $1/Z_{\text{mix}}$, is regarded as an averaged sum of the individual admittances $1/Z_{\text{part},1}$ and $1/Z_{\text{part},2}$ ²²

$$\frac{1}{Z_{\text{mix}}} = \frac{\theta_1}{Z_{\text{part},1}} + \frac{(1 - \theta_1)}{Z_{\text{part},2}} \quad (10)$$

where θ_1 is the fraction of the total capacity due to a contribution of the “small” particles.

The distributed impedance of the porous electrode, Z_{porous} , relates to the impedance of the mixed particles electrode as follows from the model of Meyers et al.²²

$$Z_{\text{porous}} = \frac{L}{\kappa + \sigma} \left[1 + \frac{2 + \left(\frac{\sigma}{\kappa} + \frac{\kappa}{\sigma} \right) \cosh \nu}{\nu \sinh \nu} \right] \quad (11)$$

with a complex parameter ν of the form

$$\nu = L \left(\frac{\kappa + \sigma}{\kappa \sigma} \right)^{1/2} \left(\frac{a}{Z_{\text{mix}}} \right)^{1/2} \quad (12)$$

where κ and σ are defined as the specific conductivities of the electrolyte solution which surrounds the particles and the solid

particles, respectively, L is the thickness of the porous electrode, a denotes the ratio between the total surface area and the volume, and Z_{mix} is obtained from eq 10.

The impedance of a parallel combination of two porous sublayers ($Z_{\text{mix},L1}$ and $Z_{\text{mix},L2}$ are the impedances of two sublayers L_1 and L_2 thick), Z_{L1+L2} , is given by the formulae similar to eq 10²³

$$\frac{1}{Z_{L1+L2}} = \frac{\theta_{L1}}{Z_{\text{mix},L1}} + \frac{(1 - \theta_{L1})}{Z_{\text{mix},L2}} \quad (13)$$

In the following modeling, we consider the case when the thicker sublayer, L_2 predominantly cover the surface of the current collector, so that $\theta_{L2} = 0.85$, thus $\theta_{L1} = 0.15$ (the general case of different ratios θ_{L1} and θ_{L2} was analyzed elsewhere²³). The set of eqs 8–13 corresponds (for the particular case of infinitely high σ and κ) to the equivalent circuit analogue shown in Figure 9b. The impedance branches for “small” and “large” particles contribute in parallel to the total electrode’s impedance, as seen in Figure 9b.

The impedance plots calculated according to eqs 8–13 (with the numerical parameters indicated in the figure’s caption) is shown in Figure 10a for the whole frequency domain with the inset enlarging the high frequency domain. In this figure, we compare impedances of the following: (i) a single “large” particle electrode (triangles), (ii) a thin porous electrode of uniform thickness ($3 \mu\text{m}$), composed of “small” and “large” particles (circles), and finally, (iii) of a geometrically nonuniform porous electrode composed of a thick ($400 \mu\text{m}$) sublayer (85%) and a much thinner sublayer, $3 \mu\text{m}$ (15% of the total electrodes’ geometric area). Note that finite (and small) values of σ and κ result in rather large active resistances at infinitely high frequencies (i.e., the effective electronic resistance of the host and the ionic resistance of the porous space filled with solution). They were subtracted from the calculated overall impedance to provide correct comparison with the impedance and the complex capacitance of the previously considered case of energetically inhomogeneous intercalation electrode.

From Figure 10a, one can see that neither the impedance of the single particle electrode nor the impedance of a thin, porous layer of a uniform thickness produce semicircles in the low-frequency domain of the spectra. In contrast, the Nyquist plot of the geometrically nonuniform porous composite electrode reveals a well pronounced LFS, which transforms, at lower frequencies, into a Warburg-type line, and finally, in the limit of the very low frequency, the $-Z''$ vs Z' plot becomes a vertical, capacitive line. In an earlier paper,²³ we presented clear evidence that the LFSs, appearing in the Nyquist plots for the geometrically nonuniform intercalation electrodes, are due to a parallel combination of the high, active resistance of the thicker sublayer and the intercalation capacitance of the thinner sublayer. The characteristic frequencies related to this semicircle are indicated in Figure 10a. Note, however, that their values depend on many factors but the major dependence is due to a different ratio between the contributions of the thicker and the thinner sublayers.²³

Figure 10b shows C'' versus C' plots calculated for the same three electrodes from the impedance spectra of Figure 10a. The first two electrodes have the complex capacitance diagram similar to that of the previously considered case of an intercalation electrode with one type of sites (FSW in Figure 7b). The complex plane capacitance diagram for the geometrically nonuniform intercalation electrode is qualitatively similar to that obtained for the single trap model (compare the related curves

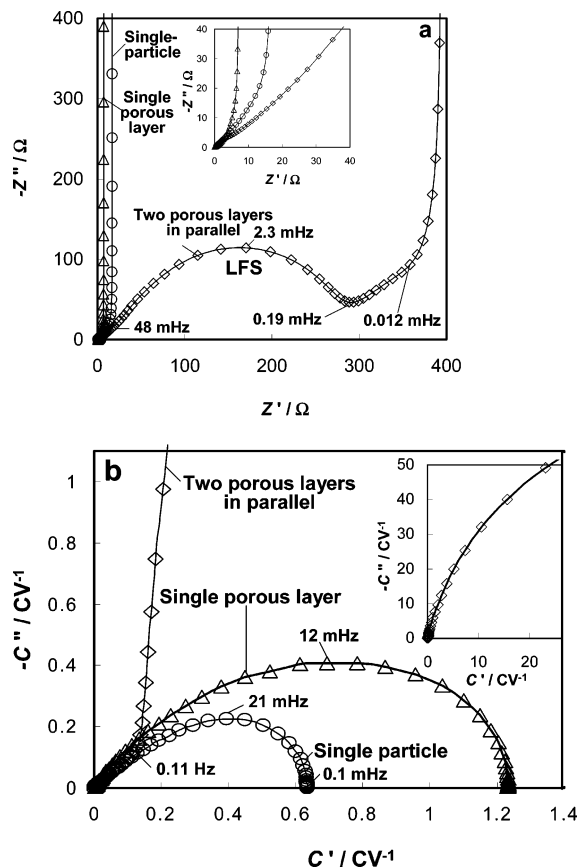


Figure 10. Theoretical impedance (a) and complex capacitance plots (b) simulated for single “large” particle electrode (triangles); for a “thin” porous homogeneous electrode ($3 \mu\text{m}$ thick) composed of “small” and “large” particles (circles) and for geometrically nonuniform porous electrode (squashed squares, equivalent circuit analogue in Figure 9b, eqs 8–13). The insets in both panels “a” and “b” are enlargements of the high frequency domains of the related impedance and capacitance spectra. Characteristic frequencies are indicated. The parameters used: “Large” particles: $R_{s,1} = 4 \mu\text{m}$, ($R_{\text{part}} = 336 \Omega\text{cm}^2$, $C_{\text{dl}} = 100 \mu\text{Fcm}^{-2}$, $R_{\text{ct}} = 88.1 \Omega\text{cm}^2$, C_{s1} and R_{s1} were formally equal to 0, i.e., the contribution due to surface films to the total impedance and capacitance was omitted for simplicity). “Small” particles: $R_{s,1} = 2 \mu\text{m}$, ($R_{\text{part}} = 84 \Omega\text{cm}^2$, all other parameters as that for “large” particles). The porous structure parameters: $a = 8.625 \times 10^3 \text{ cm}^{-1}$, $\kappa = 5.5 \times 10^{-5} \Omega^{-1}\text{cm}^{-1}$, $\sigma = 10^{-5} \Omega^{-1}\text{cm}^{-1}$, $L_1 = 400 \mu\text{m}$, $L_2 = 3 \mu\text{m}$, $\theta_{L1} = 0.15$ and $\theta_{L2} = 0.85$. Characteristic frequencies are indicated.

in Figures 10b and 7a,b). However, the related frequency dependences of C'' and C' (logarithmic coordinates) are much more informative: The plot for the single spherical particle electrode (Figure 11a) is qualitatively similar to that of a FSW element impedance (Figure 8d). The plot for the single-layer porous layer has a loop between the curves of C'' and C' vs frequency (Figure 11b) in the medium-to-high frequency domain although the effect is not very pronounced with the parameters chosen for this particular presentation. Finally, the plot of C'' and C' vs frequency for the geometrically nonuniform porous intercalation electrode has a very pronounced loop extending far in the low-frequency domain.

4. Conclusion

On the basis of the analysis of impedance and complex capacitance data of Mg ions insertion into Mo_6S_8 Chevrel phase, we showed that this is a unique system, to which the trap model fits very well. Some specific features of the crystal structure of Mo_6S_8 (inner and outer rings sites) and the divalent nature of the inserted ions lead to the existence of deep “traps” for the

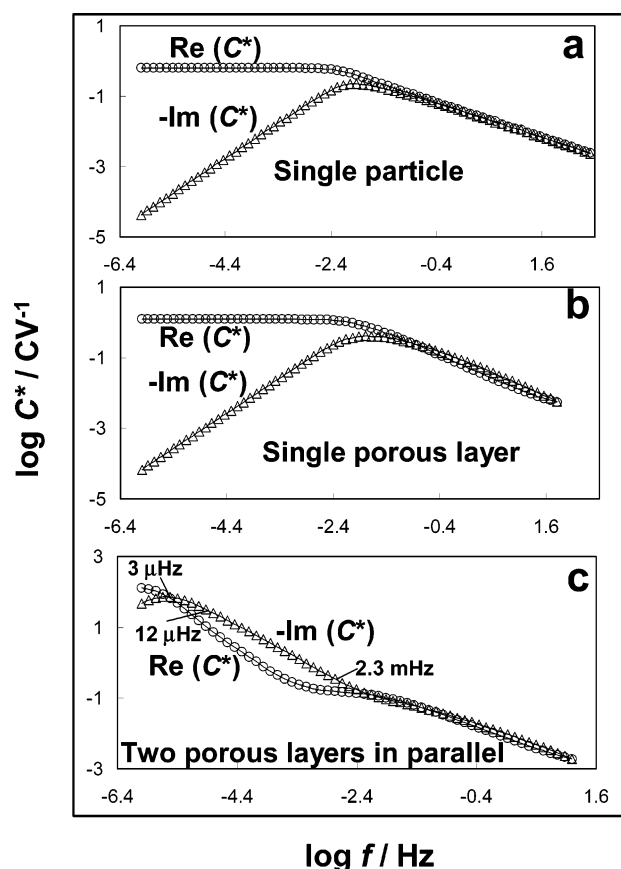


Figure 11. Real and the imaginary parts of the complex capacitance C^* as a function of frequency (in logarithmic scale) taken from the complex capacitance plots shown in Figure 10b.

initial insertion of Mg ions (which is not the case for Li ions insertion into the same host). The energy barriers of these traps decrease in the vicinity of a critical potential of 1.25 V, probably as a result of the increased electrostatic repulsion between the divalent cations. As a result, the trapped ions acquire an enhanced mobility reaching easier the transition shallow sites. The difference between the occupation of shallow sites in the thermodynamic (i.e. an equilibrium) and transition mode can be well illustrated by comparison of Mg ions insertion into Mo_6S_8 and Mo_6Se_8 Chevrel phases. Whereas the thermodynamics of the ions insertion is similar in these two hosts, the kinetics of ions insertion into Mo_6Se_8 host (for the entire range of intercalation levels) are much higher than that for Mo_6S_8 host. This can be explained by the fact that the energy barriers of the trapped ions decrease as these ions have more covalent interactions with the host's anions rather than just ionic interactions (Se^{2-} is more polarizable compared to S^{2-}); thus Mo_6Se_8 host contains only shallow sites with mobile Mg ions. The characteristic behavior of the impedance and the complex capacitance plots for $\text{Mg}_x\text{Mo}_6\text{S}_8$ in the vicinity of the above critical potential (1.25 V) was described in the framework of the single trap model the energy barrier decreasing below the critical potential, or, equivalently, expressed by an increase in the characteristic frequency of the trap sites, f_t .

We made an attempt to distinguish between the impedance response of two types of composite intercalation electrodes, which are nonuniform either in terms of the energetics of the insertion sites or in terms of their physical structure (areas of different thicknesses, different particle size, etc.). These electrodes may have very similar impedance behavior (at least qualitatively). We used for this purpose complex capacitance

diagrams, with a special emphasis on the frequency dependences of C'' and C' . The analysis revealed qualitatively similar features for the above two alternative models. The similarity can be described in terms of a parallel combination of the specific resistance and the capacitance elements which dominate the impedance response in the low-frequency domain. For electrodes with different insertion sites in the host material, single trap model that we used suggests that the dominant feature is a parallel combination of the trap resistance and the capacitance of the shallow sites (i.e., their intercalation capacitance) whereas geometric nonuniformity relates rather to their composite (physical) structure. The model of nonuniformity of intercalation electrodes that we used suggests that the dominant feature, influencing their impedance behavior, is a parallel combination of the high active resistance of the thicker parts and the intercalation capacitance of the thinner parts of the electrodes. For both types of electrodes, the low frequency impedance is purely capacitive due to both types of sites (of different energy) or due to the sum of the capacitances of the porous sublayers of different thicknesses. However, the width of the low frequency domain, in which the limiting (total) capacitances are reached, is quite different. For these two types of electrodes, this follows from the presentation of C'' and C' as a function of frequency for the two relevant models.

Very slow trapping kinetics in the single trap model results in intersecting the part of the LFS with the vertical, capacitive line in the Nyquist plots (the Warburg diffusion domain is absent in this case because of the intrinsic slowness of the trapping kinetics). In contrast, the model of geometric nonuniformity of the porous electrodes predicts an extensive Warburg region due to the thicker sublayer, which predetermines a very broad loop between the curves of C'' and C' vs frequency, which penetrates deeply into the low-frequency domain.

Acknowledgment. A partial support for this study was obtained by the ISF (Israel Science Foundation).

References and Notes

- (1) Lasia, A. *Electrochemical Impedance Spectroscopy and Its Applications, Modern Aspects of Electrochemistry*; Kluwer Academic/Plenum Publishers: Norwell, MA, 1999; Vol. 32, p 143.
- (2) Macdonald, J. R. *Impedance Spectroscopy*; Wiley: New York, 1987; p.60.
- (3) Ho, C.; Raistrick, I. D.; Huggins, R. A. *J. Electrochem. Soc.* **1980**, *127*, 343.
- (4) Armstrong, R. D. *J. Electroanal. Chem.* **1986**, *198*, 177.
- (5) Franceschetti, D. R.; Macdonald, J. R.; Buck, R. P. *J. Electrochem. Soc.* **1991**, *138*, 1368.
- (6) Mathias, M. F.; Haas O. *J. Phys. Chem.* **1992**, *96*, 3174.
- (7) Vorotyntsev, M. A.; Daikhin, L. I.; Levi, M. D. *J. Electroanal. Chem.* **1994**, *364*, 37.
- (8) Lang, G.; Inzelt, G. *Electrochim Acta* **1991**, *36*, 847.
- (9) Lang, G.; Inzelt, G. *Electrochim Acta* **1999**, *44*, 2037.
- (10) Lang, G.; Ujvari, M.; Inzelt, G. *J. Electroanal. Chem.* **1994**, in press.
- (11) Rubinstein, I.; Rishpon, J.; Gottesfeld, S. *J. Electrochem. Soc.* **1986**, *133*, 729.
- (12) Bisquert, J. *J. Electroanal. Chem.* **2001**, *499*, 112.
- (13) Vorotyntsev, M. A.; Deslouis, C.; Musiani, M. M.; Tribollet, B.; Aoki, K. *Electrochim Acta* **1999**, *44*, 2105.
- (14) Vorotyntsev, M. A.; Badiali, J.-P.; Inzelt, G. *J. Electroanal. Chem.* **1999**, *472*, 7.
- (15) Zoltowski, P. *J. Electroanal. Chem.* **1994**, *375*, 45.
- (16) Pajkossy, T. *J. Electroanal. Chem.* **1994**, *364*, 111.
- (17) Montella, C. *J. Electroanal. Chem.* **2002**, *518*, 61.
- (18) Levi, M. D.; Aurbach, D. *Electrochim. Acta* **1999**, *45*, 167.
- (19) Bisquert, J.; Vikhrenko, V. S. *Electrochim. Acta* **2002**, *47*, 3977.
- (20) Bisquert, J. V. S. *Electrochim. Acta* **2002**, *47*, 2435.
- (21) Bisquert, J. V. S. *J. Phys. Chem.* **2002**, *106*, 325.

- (22) Meyers, J. P.; Doyle, M.; Darling, R. M.; Newman, J. *J. Electrochem. Soc.* **2000**, *147*, 2930.
- (23) Levi, M. D.; Aurbach, D. *J. Phys. Chem.* **2004**, *108*, 11693.
- (24) Levi, M. D.; Lancry, E.; Gizbar, H.; Lu, Z.; Levi, E.; Gofer, Y.; Aurbach, D. *J. Electrochem. Soc.* **2004**, *151*, A1044.
- (25) Levi, M. D.; Lancry, E.; Gizbar, H.; Gofer, Y.; Levi, E.; Aurbach, D. *Electrochim. Acta* **2004**, *49*, 3201.
- (26) Levi, M. D.; Gizbar, H.; Lancry, E.; Gofer, Y.; Levi, E.; Aurbach, D. *J. Electroanal. Chem.* **2004**, *569*, 211.
- (27) Chusid, O.; Gofer, Y.; Gizbar, H.; Vestfrid, Y.; Levi, E.; Aurbach, D.; Riech, I. *Adv. Mater.* **2003**, *15*, 627.
- (28) Yvon, K. In: *Current Topics in Material Science*; Kaldis, E., Ed.; North-Holland Publishing Company: Amsterdam, 1979; vol. 3, p 53.
- (29) Uchida, T.; Tanjo, Y.; Wakihara, M.; Taniguchi, M. *J. Electrochem. Soc.* **1990**, *137*, 7.
- (30) Levi, M. D.; Lancry, E.; Levi, E.; Gizbar, H.; Gofer, Y.; Aurbach, D. *Sol. St. Ionics*, in press.
- (31) West, A. R. *Basic Solid State Chemistry*; Wiley & Sons: Chichester, New York, Brisbane, Toronto, Singapore, 1988; 415 pp.
- (32) Aurbach, D.; Markovski, B.; Weissman, I.; Levi, E.; Ein-Eli, Y. *Electrochim. Acta* **1999**, *67*, 45.